In-Situ X-ray Deformation Study of Fluorinated Multiwalled Carbon Nanotube and Fluorinated Ethylene−Propylene Nanocomposite Fibers

Xuming Chen, Christian Burger, Dufei Fang, Igors Sics, Xuefen Wang, Weidong He, Rajesh H. Somani, Kyunghwan Yoon, Benjamin S. Hsiao,* and Benjamin Chu*

Department of Chemistry, Stony Brook University, Stony Brook, New York 11794-3400

Received January 24, 2006; Revised Manuscript Received May 1, 2006

ABSTRACT: A fluorinated multiwalled carbon nanotube (FMWNT) was prepared by reaction of 3-perfluorooctylpropylamine with carboxylic acid groups on the oxidized carbon nanotube surface. The modification was confirmed by TGA, TEM, and solubility tests in a perfluorodecalin solvent. Nanocomposite fibers based on FMWNT and a fluoro-ethylene−propylene (FEP) copolymer were fabricated by melt blending and melt spinning. SEM examination indicated that the dispersion of FMWNT in FEP was significantly better than that of the as-received multiwalled carbon nanotube (MWNT) in FEP. Both yield strength and modulus of the melt-spun FMWNT/FEP nanocomposite fiber increased with increasing FMWNT content, but the elongation-to-break ratio decreased. In-situ small-angle X-ray scattering (SAXS) and wide-angle X-ray diffraction (WAXD) techniques were used to follow the structural changes during tensile deformation of melt-spun fibers. In pure FEP fibers, perpendicularly arranged lamellar stacks (with respect to the fiber axis) became tilted at small strains, while destruction of lamellae took place at high strains (>250%), resulting in the rapid decrease of crystallinity. Surprisingly, the tilting of lamellar stacks was not observed in FEP/FMWNT nanocomposite fibers during deformation. We hypothesize that the well-dispersed FMWNT particles form a fibrous network, which can carry a significant fraction of local stress, resulting in overall increases of yield strength and modulus. A possible mechanism to explain the effect of FMWNT on the lamellar structural change in FEP and corresponding mechanical behavior is presented.

Introduction

Carbon nanotubes (CNTs) have an array of extraordinary mechanical, thermal, and electrical properties, making them extremely desirable to be incorporated in polymer nanocomposites for a wide range of applications.[1−3] In our laboratory, we are particularly interested in a specific class of polymer nanocomposites containing CNTs and fluoropolymers (e.g., poly(tetrafluoroethylene) (PTFE), fluoro-ethylene−propylene (FEP) copolymer, and perfluoroalkoxy (PFA) copolymer). The unique structure of CNTs can overcome several shortcomings of fluoropolymers, such as relatively poor mechanical properties and difficulty in processing,[4−7] without compromising their unique properties, such as chemical inertness and low surface tension. However, the dispersion of CNTs in fluoropolymers is usually difficult because of the low matrix surface tension.[6,8] Surface modification turns out to be an effective means to enhance the compatibility of CNTs and fluoropolymers and thus the dispersibility.[9−12] Nakajima et al. were the first group to report the side-wall functionalization of multiwalled carbon nanotube (MWNT) using elemental fluorine.[13] This class of fluorinated MWNT has been further studied by several other groups subsequently.[14−16] Mickelson et al. also demonstrated a similar approach to carry out fluorination of a single-walled carbon nanotube (SWNT).[17]

It is important to note that the surface properties of CNTs modified directly with elemental fluorine (the modified compounds are sometimes termed fluorotubes) are very different from those modified with fluorinated alkyl chains (e.g., alkyl fluorides). For example, the X-ray photoelectron spectroscopy (XPS) examination of SWNT modified with alkyl fluorides exhibited an F 1s peak with a binding energy of 687 eV, whereas that of poly(tetrafluoroethylene) showed an F 1s binding energy of 691.5 eV.[18] This suggests that fluorine on the surface of fluorotubes is considerably more ionic than fluorine in alkyl fluorides. Thus, the increasing ionic nature of the C−F bond in fluorotubes appears to make the fluorine component more chemically reactive and easier to form hydrogen bonds with alcohols than that in alkyl fluorides attached to SWNT.[19] This hypothesis was confirmed by another study,[20] where the fluorine displacement reaction was used to functionalize CNTs with other group-terminated moieties. Recently, Dunitz and Howard studied the hydrogen-bonding capability of alkyl fluorides, and they concluded that the fluorine components in such species are poor hydrogen bond acceptors.[21,22] In other words, the alkyl fluorides attached on the CNT surface have very similar properties as the chain segments in fluoropolymers. This implies that CNTs functionalized with alkyl fluorides should have good compatibility with or good dispersibility in the fluoropolymer matrix.

In this study, MWNT was fluorinated by chemical attachment of short alkyl fluoride chains to the oxidized surface. MWNT was chosen because while its oxidized surface can be reacted and produced a dense layer of alkane fluoride chains, the inner structure of carbon layers is retained during the modification process. Results from this study confirmed that the fluorinated MWNT (FMWNT) could be easily dispersed in melt-processable fluoropolymers, such as FEP, by conventional melt-mixing methods. Herein, we are mainly interested in understanding the relationship between the structure (i.e., crystal structure of FEP and nanofibrous morphology) and property (mechanical) during deformation of FMWNT/FEP nanocomposites.

A FEP copolymer (i.e., a copolymer of polytetrafluoroethene and hexafluoropropylene) was selected as the matrix material because it has a relatively low melting point (about 260 °C) and it is melt-processable. The chain architecture, crystal

* To whom correspondence should be addressed: Tel (631) 632-7793 (Hsiao), (631) 632-7928 (Chu); Fax (631) 632-6518; e-mail bhsiao@notes.cc.sunysb.edu (Hsiao), bchu@notes.cc.sunysb.edu (Chu).

10.1021/ma060173u CCC: $33.50
Published on Web 07/11/2006

structure, and general physical properties of FEP are similar to those of PTFE, but its molecular weight and crystallinity are notably lower than that of PTFE.[6,7] For example, FEP also has a low friction coefficient and a high dielectric constant; it has been used in many applications, such as industrial and medical tubing, film, and insulation.[6] We hypothesize that the presence of short alkane fluoride chains on the FMWNT surface can lead to some changes in the crystal structure and morphology of the FEP matrix and thus the corresponding mechanical properties. This hypothesis was verified by in-situ small-angle X-ray scattering (SAXS) and wide-angle X-ray diffraction (WAXD) studies of FMWNT/FEP nanocomposites during tensile deformation using synchrotron radiation. Results from this study provided useful information for preparation of high-performance CNT/PTFE nanocomposites, where PTFE has much higher molecular weight and crystallinity than FEP. Recently, we have demonstrated a unique class of tough nanocomposite containing carbon nanofiber (MCNF) modified with short alkyl chains and ultrahigh molecular weight polyethylene (UHMWPE).[23] The mobile hydrocarbon layers in the UHMWPE/MCNF interface appear to be the key to overcome the barrier of high chain entanglements in the solid UHMWPE matrix and to induce significantly enhanced elongation-to-break ratio (thus toughness). The molecular weight of UHMWPE is similar to that of PTFE.

Experimental Section

Samples and Preparation. The MWNT sample was obtained from the Nanostructrued and Amorphous Materials, Inc. The chosen MWNT sample was produced by the catalytic chemical vapor deposition method. The diameter of the MWNT was about 8−15 nm, and the purity was greater than 95%. The as-received MWNT sample was first oxidized using a concentrated H_2SO_4/HNO_3 mixture (3:1). The subsequent fluorination procedures were carried out as follows. 0.5 g of oxidized MWNT was reacted with 2 g of 3-perfluorooctylpropylamine (from Fluorous Technologies, Inc.) with a boiling point of about 130 °C. The mixture was gently stirred and maintained at 120 °C under nitrogen for 7 days to complete the reaction. The resulting mixture was washed with chloroform, THF, and alcohol several times and filtered with a 0.1 μm pore membrane under vacuum. The recovered fluorinated MWNTs (FMWNT) were dried in a vacuum at 70 °C. The weight of the final product was recorded carefully to determine the effectiveness of the fluorination procedure. TGA thermograms of FMWNT and MWNT (as a reference) samples were collected at a heating rate of 30 °C/min using a TGA 7 (Perkin-Elmer Inc.). Transmission electron microscopy (TEM) images of FMWNT and MWNT were collected using the TEM JEOL 1200EX instrument.

The preparation of the FMWNT/FEP (or MWNT/EFP as a control) nanocomposite samples was carried out as follows. FMWNT (MWNT) was first mixed with FEP particles (Teflon FEP 100 from Dupont) at room temperature. The solid mixture was then melt-blended in a twin-screw blender (DACA Instruments) at 280 °C for 10 min. A total of four nanocomposite samples were prepared: three samples contained 0.5, 1, and 5 wt % of FMWNT and one sample contained 0.5 wt % of as-received MWNT. One pure FEP sample was also prepared using the same procedures outlined above. Nanocomposite or pure FEP fibers were melt spun by a custom-built press-spinning unit developed by Dow scientists[24,25] and modified by us. The detailed instrumentation design and the operating procedure were described elsewhere.[26] In brief, the spinneret diameter was 0.7 mm, the spin-draw ratio was set at 1.0, and the spinning temperature was set at 290 °C. The surface and cross-section views of the nanocomposite fibers were examined by scanning electron microscopy (SEM, LEO1550, LEO, USA). For the preparation of the cross-section view, the fibers were fractured in liquid nitrogen.

Characterization. Small strain oscillatory shear measurements in the linear viscoelastic region of the nanocomposite melts were determined by using a strain-controlled rheometer (Anton-Paar Physica MCR 301) equipped with a parallel plate sample holder (diameter 25 mm). The measurements were carried out at 280 °C. A constant strain amplitude (=1%) was employed in all dynamic measurements. The chosen frequency scan was $0.05 < \omega < 100$. Dry nitrogen was used to suppress the oxidative degradation process of melts at high temperatures.

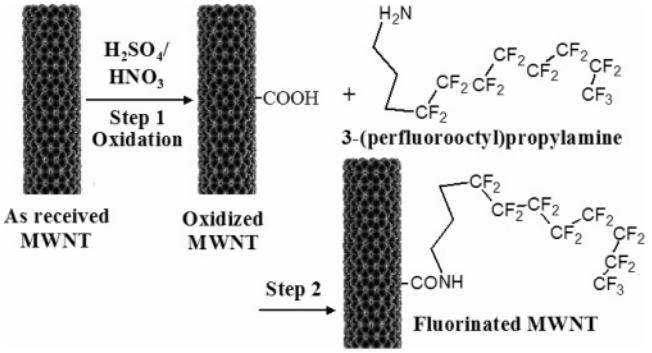

Figure 1. Chemical modification schemes for fluorination of MWNT.

In-situ wide-angle X-ray diffraction (WAXD) and small-angle X-ray scattering (SAXS) experiments were carried out at the X27C beamline in the National Synchrotron Light Source (NSLS), Brookhaven National Laboratory (BNL). The details of the experimental setup at the X27C beamline have been reported elsewhere.[27] The wavelength used was 0.13 nm. A three-pinhole collimation system was used to define the incident beam from a double multilayered monochromator. The sample-to-detector distance for WAXD was 100.5 mm and for SAXS was 1884.3 mm. A two-dimensional (2D) X-ray detector MAR-CCD (MAR, Inc.) was used for data collection. A typical image acquisition time was 15 s per image. The sample was uniaxially stretched using a modified Instron 4442 tensile apparatus, with which symmetric deformation was carried out. The initial length between the Instron jaws was 10 mm. The samples were enclosed in an environmental chamber during experiment; all experiments were carried out at room temperature (ca. 23 °C). The chosen stretching speed was 5 mm/min. 2D SAXS/WAXD images were corrected for the beam fluctuations, sample thickness, and background scattering from air/instrument. The WAXD images were additionally corrected for the effect of the curvature from the Ewald sphere (i.e., Fraser correction[28]). The Hermans' orientation factors ($\bar{P}_2$) were calculated from the equatorial peaks from the WAXD patterns.

Results and Discussion

Surface Fluorination of MWNT and Characterization. Figure 1 illustrates the schematic diagram for fluorination of MWNT. The as-received MWNT was first oxidized to generate acidic groups on the surface that include hydroxyl groups, lactone groups, and carboxylic acid groups. The total concentration of the acidic groups was about 4.3 mmol/g, which was determined by using a standard titration method.[29] The addition of 3-perfluorooctylpropylamine reacted with the carboxylic acid groups and formed 3-perfluorooctylpropylamide, as shown in Figure 1. The weight of FMWNT, indicative of the effectiveness of thermal reaction for surface grafting of 3-perfluorooctylpropylamide, was 1.2 g, which was an increase of about 0.7 g from the initial weight of oxidized MWNT (0.5 g). This observation confirmed that the amidation reaction took place and fluoride alkyl chains on the FMWNT surface were formed. These results are consistent with the observations of Huang and Fernando,[30,31] who studied the acylation−amidation thermal reaction for functionalization of SWNT using diamine-terminated poly(ethylene glycol). Their results showed that thermal reaction was more effective than EDAC-activated coupling.

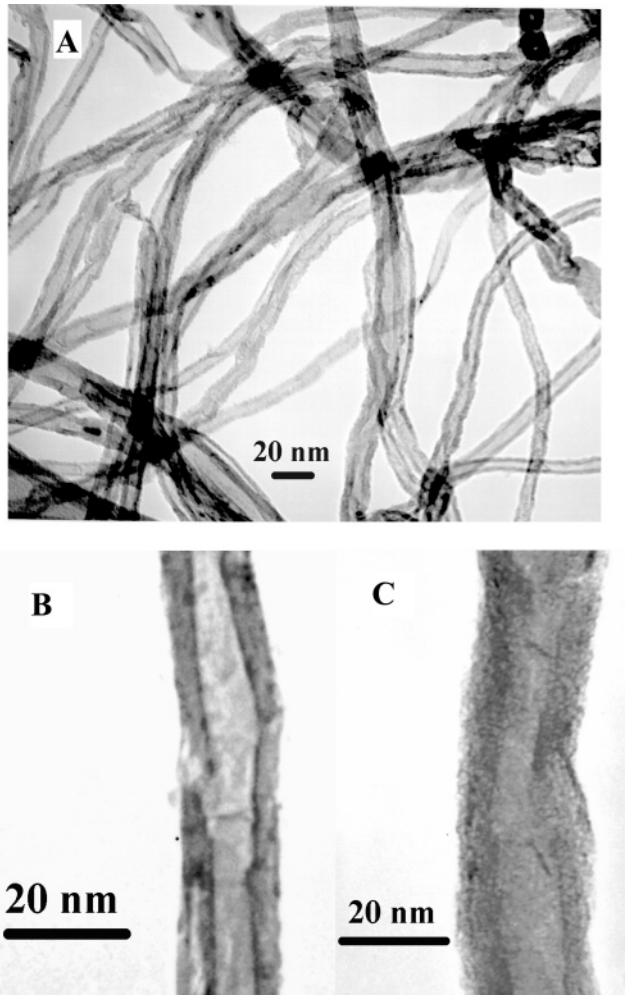

Figure 2. TEM micrographs of (A) and (B) MWNT at different magnifications and (C) FMWNT.

TEM images of MWNT and FMWNT samples are illustrated in Figure 2. The surface of the as-received MWNT was relatively clean, and their diameter was in the range of 10−20 nm (Figure 2A). The enlarged view of the FMWNT sample is shown in Figure 2B, which indicates the existence of a sharp edge. Figure 2C illustrates the surface of FMWNT modified with 3-perfluorooctylpropylamide. The blurred and dark edge as well as the dark core structure (from side projection) is consistent with the existence of a layer of 3-perfluorooctylpropylamide attached to the surface of MWNT. The attached layer seemed to be quite uniform on the surface of FMWNT.

The thermal stability of the as-received MWNT, oxidized MWNT, and FMWNT was determined by thermogravimetric analysis (TGA), where results are shown in Figure 3. The as-received MWNT exhibited a higher thermal stability than those of oxidized-MWNT and FMWNT. The FMWNT thermogram showed a distinct and significant weight loss in the range 300−600 °C. The initial weight loss, near 300 °C, could be attributed to the decomposition of 3-perfluorooctylpropylamide molecules, while the later weight loss (close to 600 °C) could be attributed to the decomposition of MWNT. From the weight loss in the FMWNT thermogram, the weight fraction of the surface attached 3-perfluorooctylpropylamide was about 60% (the estimation was carried out using the first derivative of the thermogram, data not shown). It was found that the attached 3-perfluorooctylpropylamide molecules were completely degraded at 550 °C, at a value much higher than the decomposition temperature of octadecylamide groups at about 400 °C.[23] The

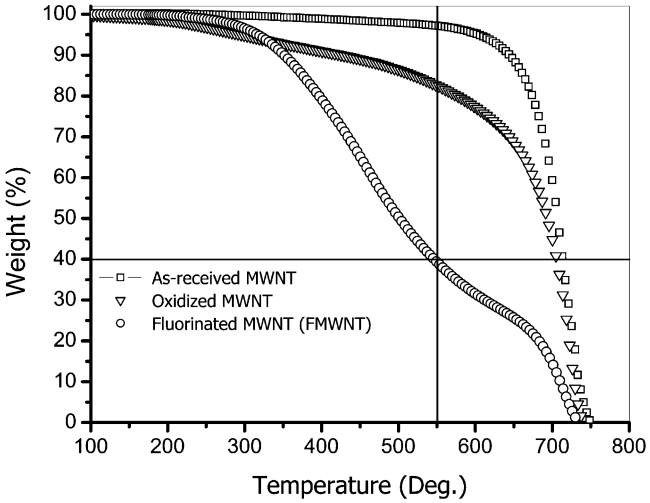

Figure 3. TGA thermograms of the as-received MWNT, oxidized MWNT, and FMWNT samples.

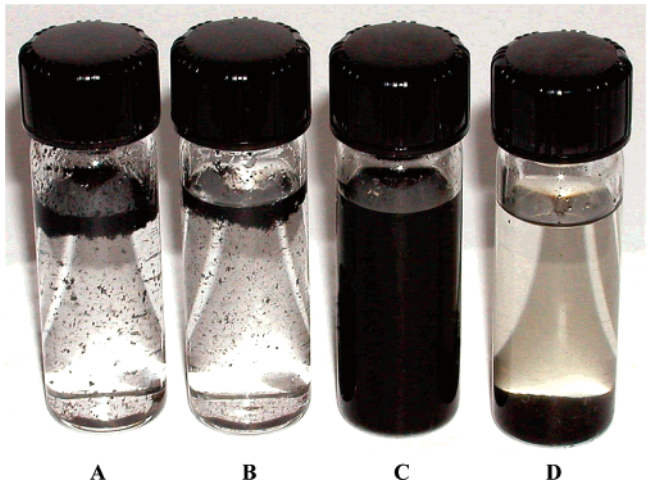

Figure 4. Dispersion of (A) as-received MWNT, (B) oxidized MWNT, and (C) FMWNT in perfluorodecalin as well as (D) FMWNT in 2-propanol. (All samples were prepared by 5 min of sonication and subsequently equilibrated for 12 h; (C) could stay at a homogeneous state for months without visual change.)

higher decomposition temperature of 3-perfluorooctylpropylamide was due to the chemical inertness of fluoroctyl groups vs octadecylamide groups.

The dispersibility of the as-received MWNT, oxidized MWNT, and FMWNT in perfluorodecalin is shown in Figure 4. The MWNT and oxidized MWNT could not be dispersed in perfluorodecalin (the absence of a stable suspension in Figure 4A,B). In fact, the compatibility of MWNT or oxidized MWNT with perfluorodecalin was so low that as soon as sonication was stopped both suspensions were quickly separated into two layers. With the density of perfluorodecalin (about 1.9 g/mL) being higher than that of MWNT and of oxidized MWNT (both about 1.5 g/cm^3), the MWNT (or oxidized MWNT) layer floated on top of the perfluorodecalin layer. On the other hand, FMWNT dispersed very well in perfluorodecalin and formed a homogeneous suspension, as seen in Figure 4C. This observation indicated the strong compatibility between FMWNT (modified with 3-perfluorooctylpropylamine) and the perfluorodecalin solvent. As a test to determine whether the fluorides on FMWNT could form hydrogen bonds with alcohol, FMWNT was dispersed in 2-propanol under the same dispersion conditions. Figure 4D shows that phase separation occurred between FMWNT and 2-propanol, indicating the absence of solubility

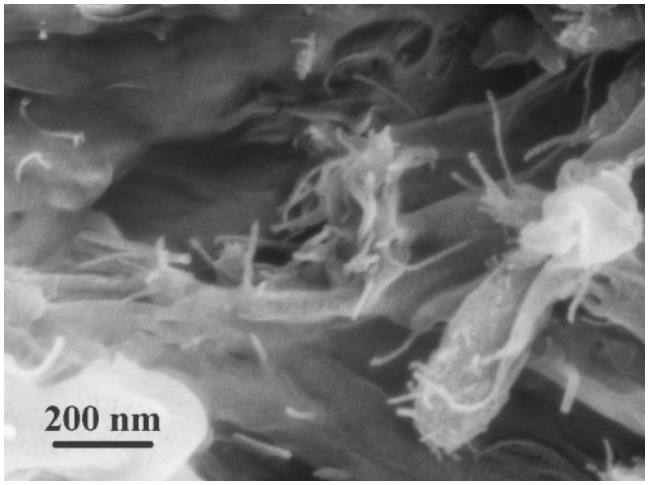

Figure 5. Representative SEM micrograph of the fractured 5 wt % FMWNT/FEP nanocomposite fiber cross section.

or the lack of hydrogen-bonding ability between the fluorides on FMWNT and 2-propanol. The solubility test results of FMWNT were in contrast with the study by Mickelson et al.,[19] who found that fluorinated SWNT could not be dissolved in perfluorinated solvents even with the "like dissolves like" approach using the procedures of sonication and heating. They concluded that the fluorotubes would not have good compatibility with tetrafluoroethylene polymers. The noted difference can be attributed to the discrepancy between fluorotubes (i.e., SWNT modified with elemental fluorine) and FMWNT (i.e., MWNT attached with 3-perfluorooctylpropylamide). As mentioned earlier, the fluorine component attached to SWNT is considerably more ionic and chemically active. The fluorotubes can be molecularly dispersed in a variety of alcohols due to formation of hydrogen bonds between them, but FMWNT appears to be difficult to form hydrogen bonding with alcohol (at least 2-propanol), as indicated in Figure 4D.

Morphology and Mechanical Properties of FMWNT/FEP Nanocomposites. Figure 5 shows SEM micrographs of the fractured surfaces of FMWNT/FEP nanocomposites. The dispersion of the as-received MWNT in FEP was very poor. Even at a concentration of 0.5 wt %, MWNTs formed large aggregates in FEP. However, the dispersion of FMWNT in FEP was significantly better than that of the as-received MWNT, even when the FMWNT content was increased to 5 wt % (Figure 5). It was seen that the aggregates of FMWNT (bundle-like) were also present in these nanocomposites; however, their sizes were very small. Many single filaments of FMWNT were well dispersed in the FEP matrix, which was clearly observed in Figure 5.

Figure 6 illustrates the strain−stress curves of the pure FEP fiber, MWNT/FEP, and FMWNT/FEP nanocomposite fibers. The tensile strength and elongation properties of the FMWNT/FEP fiber were much higher than that of the MWNT/FEP fiber (Figure 6A). This can be attributed to the good dispersion of FMWNT in FEP and the possible existence of interfacial adhesion between FMWNT and FEP. The yield strength of the nanocomposite fiber increased with the increasing FMWNT content (Figure 6B). However, the corresponding elongation-to-break ratio decreased, perhaps because at high loadings of FMWNT, the particle dispersion became poorer in the polymer matrix. The existence of small FMWNT aggregates was seen in Figure 5, and they would decrease the elongation of the nanocomposite. At low loadings of FMWNT, the particle dispersion was good, resulting in nanocomposites with good

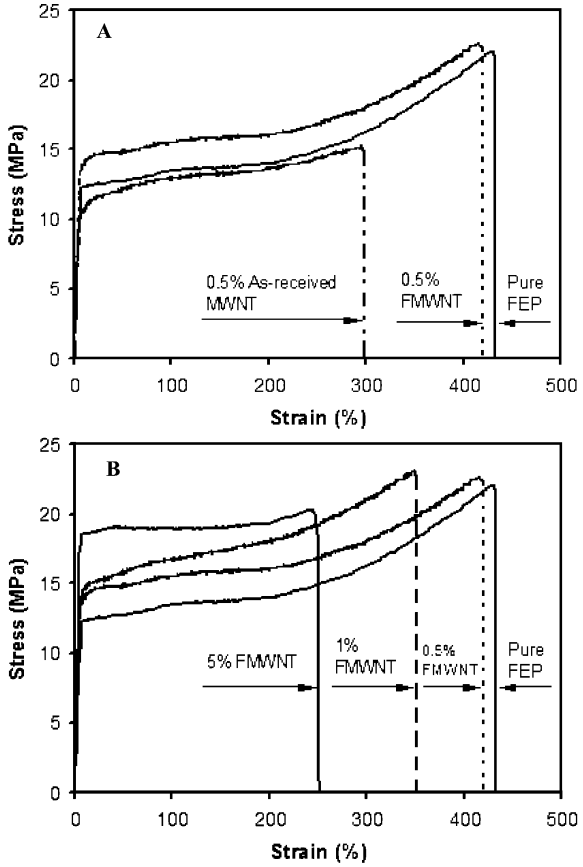

Figure 6. Strain−stress curves of (A) pure FEP, MWNT/FEP, and F-MWNT/FEP nanocomposite (all with 0.5 wt % particle loading) fibers and (B) the F-MWNT/FEP fibers having different filler concentrations (0, 0.5, 1, and 5 wt %) at room temperature.

mechanical properties. Thus, the nanotube dispersion appeared to be a critical factor affecting the elongation-to-break ratio of the nanocomposite. It is clear that, with the present surface modification scheme, higher loading of FMWNT (e.g., >5 wt %) would lead to aggregation of FMWNT because the overall miscibility between FMWNT and FEP is not too high (note that MWNT is not miscible with FEP) even though the grafted surface layer on FMWNT is compatible with the polymer matrix. In addition, the melt-mixing procedure adopted in this study might also be partly responsible for the aggregation of FMWNT in FEP, since the present shear conditions could only be considered moderate.

Figure 7 shows the storage moduli (G') for FEP and FMWNT/FEP melts at 280 °C. The storage modulus of the 0.5 wt % MWNT/FEP sample was very similar to that of pure FEP in the whole frequency region. However, the storage modulus of the 0.5 wt % FMWNT/FEP sample was higher than those of pure FEP and 0.5 wt % MWNT/FEP samples. The significant increase in the storage modulus of the 0.5 wt % FMWNT/FEP sample was mainly due to the better dispersion of FMWNT in FEP, which was consistent with tensile properties in Figure 6. In Figure 7, the 5 wt % FMWNT/FEP sample exhibited a higher storage modulus than the 0.5 wt % FMWNT/FEP sample. However, the corresponding increase of the storage modulus at high frequency (ω > 30 1/s) was found to slow down, which might be due to the possible slip between FEP (and nanocomposite) and parallel-plate sample holder at high frequency, since FEP has a low friction coefficient.

In-Situ Wide-Angle X-ray Diffraction Study during Deformation. The crystal structure of PTFE can display three

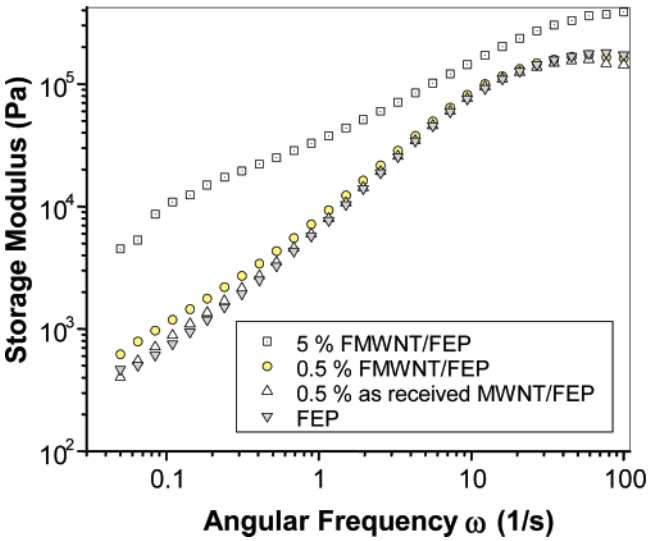

Figure 7. Thermorheological responses of FEP, FMWNT/FEP, and MWNT/FEP nanocomposites at 280 °C.

different polymorphisms at one atmospheric pressure. Below 292 K, PTFE exhibits the phase II structure with a triclinic unit cell; above 303 K, PTFE exhibits the phase I structure with a hexagonal unit cell; between 292 and 303 K, PTFE exhibits the phase IV structure with a hexagonal unit cell.[32−35] The general crystal structure of FEP was also well characterized by X-ray diffraction,[36−41] and it is similar to PTFE even though the corresponding transition regions are not the same. For example, Weeks et al. reported that the incorporation of perfluoromethyl groups could shift the transition to lower temperatures.[37] For a FEP copolymer with about 3.4 CF_3 per 100 main-chain carbon atoms, only one transition between 229 and 243 K was reported.[38] The higher temperature phase I structure of FEP is quite similar to that of PTFE, except that the FEP phase I structure possesses a longitudinal disorder along the chain axis due to the incorporation of perfluoromethyl groups.[38] The chosen FEP sample (FEP 100) in this study contained about 13 mol % hexafluoropropylene (HFP),[36] whereby the CF_3 concentrations were about 6.5 per 100 main-chain carbon atoms. Thus, the structure in the chosen FEP at room temperature was phase I with a large degree of longitudinal disorder.

A representative 2D WAXD pattern of the 5 wt % FMWNT/FEP fiber collected at a strain of 60% during deformation is shown in Figure 8A. In general, the WAXD patterns collected from FMWNT/FEP nanocomposite fibers (e.g., 0.5 and 5 wt %) during deformation were very similar to those of pure FEP fiber. From the positions of three diffraction peaks in the WAXD pattern (Figure 8A)—(100), (110), and (200)—the FEP crystal structure at room temperature (23 °C) can be described by a hexagonal unit cell with a being about 0.57 nm. In Figure 8A, a distinct reflection from the stacking of graphene layers in MWNT could also be identified at $d = 0.34$ nm. In hexagonal graphite, this reflection would be indexed as (002) (hereafter, this notation was kept although it does not exactly apply to MWNT). The (002) reflection exhibited a higher intensity along the equatorial direction compared to the meridional direction in the deformed sample, indicating that FMWNT in the FEP fiber became oriented along the stretching direction. This aspect will be discussed in detail later.

Figure 8B illustrates selected 2D WAXD patterns of pure FEP fiber at varying strains during tensile deformation at room temperature (we note that the general features of WAXD patterns from FEP were similar to those of FMWNT/FEP, which are not shown here). These results indicate that the presence of FMWNT did not change the basic crystal structure (i.e., a hexagonal unit cell) of FEP. In Figure 8B, the (100) diffraction intensity became aggregated around the equator with increasing strain, whereby a pair of sharp pointlike (100) diffraction peaks were seen at high strains (e.g., 410%). The (110) and (200) reflections exhibited a similar change on the equator. In addition, a broad diffraction peak with position in the s range of 4−4.8 nm^{-1} (i.e., $d = 2.5$−2.1 nm) was seen, which was related to a

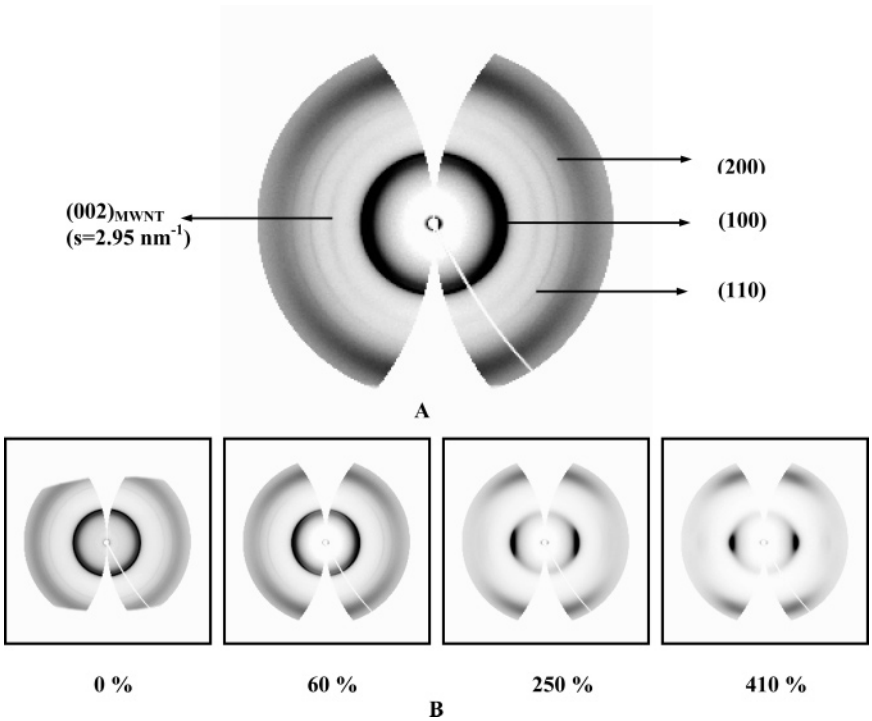

Figure 8. (A) A typical WAXD pattern of 5 wt % FMWNT/FEP nanocomposite fiber and (B) selected WAXD patterns of pure FEP fibers collected during deformation at different strains.

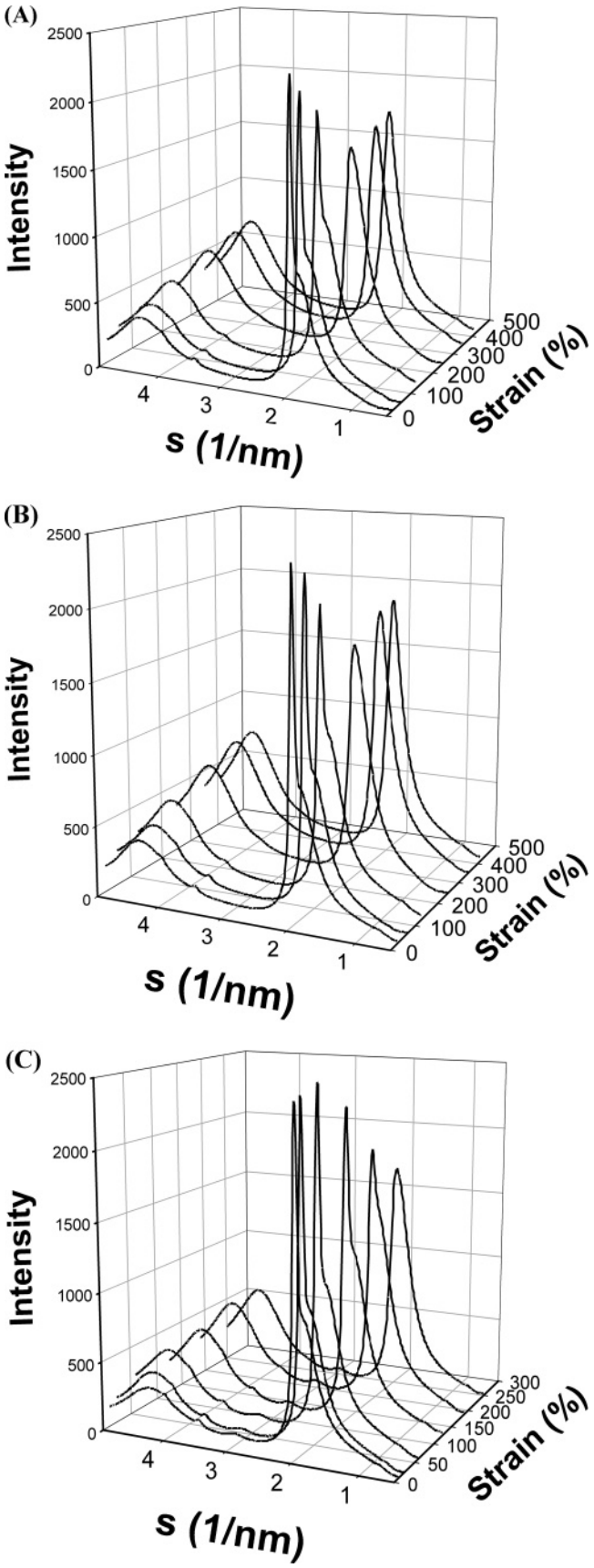

Figure 9. Integrated 1D WAXD intensity profiles of (A) pure FEP, (B) 0.5 wt % FMWNT/FEP nanocomposite fiber, and (C) 5 wt % FMWNT/FEP nanocomposite fiber during stretching at room temperature.

one zigzag repeat unit in the trans conformation of the FEP chains.

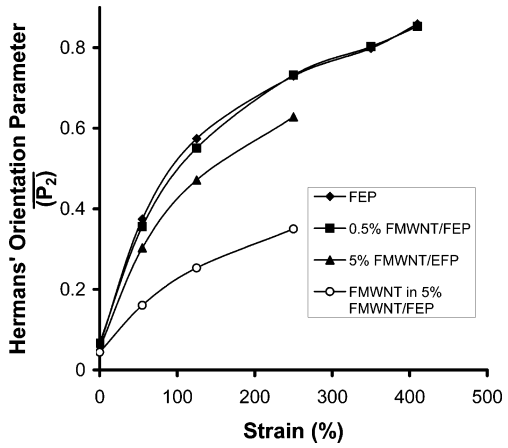

Figure 10. Changes of Hermans' orientation parameter $\bar{P}_2$ for FEP and FMWNT/FEP nanocomposite (0.5 and 5 wt %) fibers and that for FMWNT in the 5 wt % FMWNT/FEP fiber during stretching at room temperature.

Selected circularly integrated 1D intensity profiles from Fraser-corrected 2D WAXD patterns of pure FEP, 0.5 wt % FMWNT, and 5 wt % FMWNT nanocomposite fibers during deformation at different strains are shown in parts A, B, and C of Figure 9, respectively. In these figures, the intensity was normalized by beam fluctuations and sample thickness; thus, the height of the strongest reflection peak (100) at $s = 2.04$ nm^{-1} could be considered as a marker to estimate the crystallinity index (hereafter, referred to as crystallinity). The initial height of the strongest (100) reflection increased slightly with increasing FMWNT, indicating that the presence of FMWNT probably nucleated some extra FEP crystals in the composites. In pure FEP fiber (Figure 9A), the height of the (100) peak decreased rapidly at strains below 250%, which could be attributed to a mechanical melting process that destroyed some crystals through the chain-pulling mechanism. At strains larger than 250%, the height of the (100) peak increased slightly, suggesting the process of strain-induced crystallization. The above results are consistent with those observed in PTFE during stretching.[42] For the 0.5 wt % FMWNT nanocomposite fiber (Figure 9B), a similar trend of diffraction profile change was observed as for pure FEP, although the profile exhibited a slightly slower decrease of crystallinity at the initial stages (e.g., strain < 60%). This observation suggests that the low loading of FMWNT does not carry much of the applied stress, where the crystal structure and morphology of FEP are primarily responsible for the mechanical response during stretching. Contrary to the observations in Figure 9A,B, Figure 9C revealed that the crystallinity increased slightly at the initial stage of deformation (e.g., strain <60%) and decreased sharply afterward for the 5 wt % FMWNT nanocomposite fiber. This unusual behavior may be explained by the following argument. It is conceivable that more crystals are generated in the presence of large FMWNT concentration than those being destroyed by mechanical melting during the initial stage of deformation. Furthermore, since the surface layer of FMWNT is compatible with the FEP matrix, the filler can effectively bear the local stress, thus reducing the overall stress on the FEP chains. This can also result in a smaller degree of crystal destruction. Nevertheless, the large extension of polymer chains would still induce crystallization of FEP at higher strains.

Degree of Crystal Orientation. The changes in degree of crystal orientation for the FEP matrix during stretching can be quantified by using the Hermans' orientation parameter, $\bar{P}_2 = \{(3\langle\cos^2\phi\rangle - 1)/2\}$, where $\bar{P}_2$ is defined by the orientation

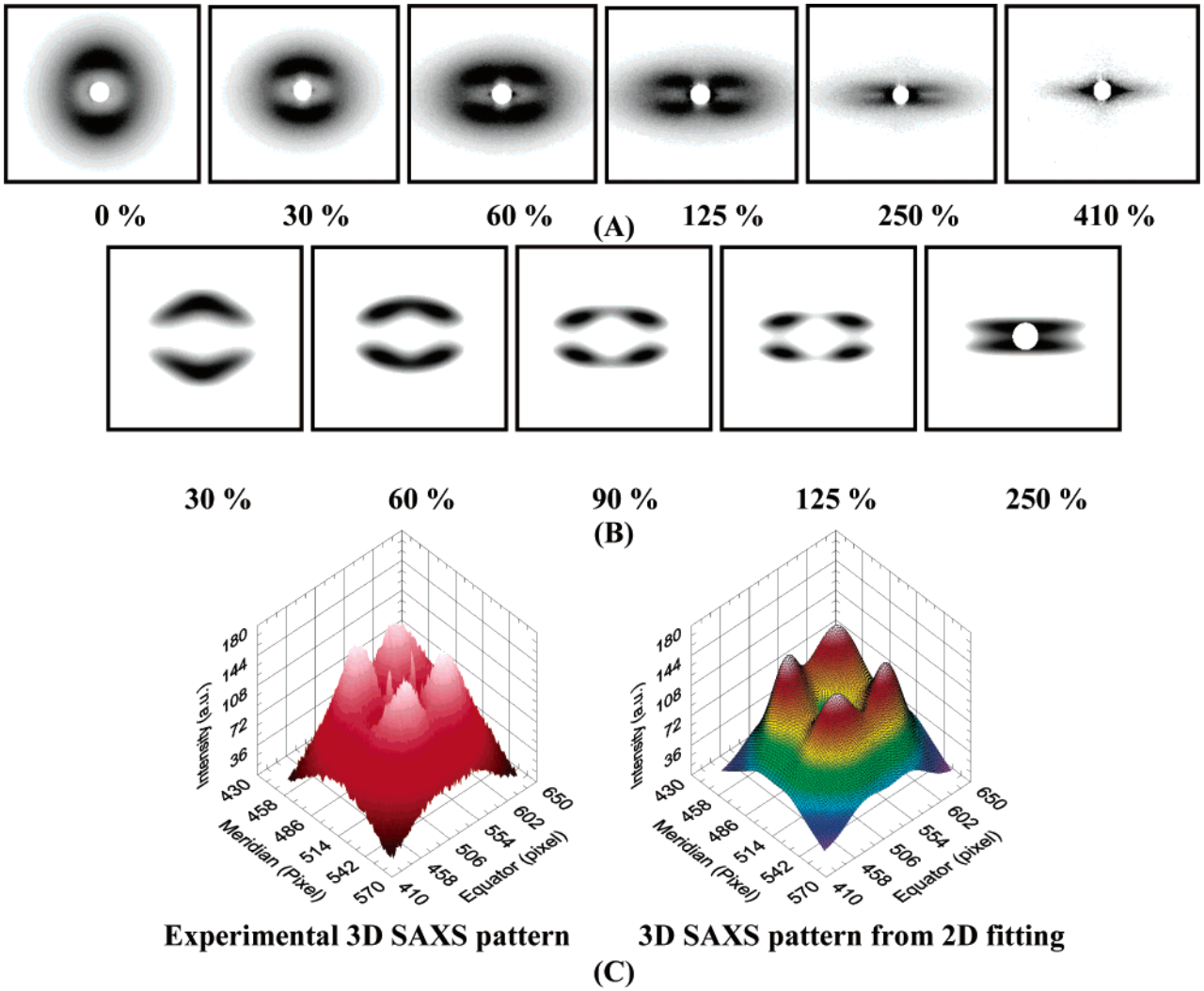

Figure 11. (A) SAXS patterns of the pure FEP fiber during stretching, (B) simulated SAXS patterns from the 2D fitting data at different strains, and (C) typical 3D SAXS profiles from experimental and fitting results (strain of 90%).

distribution function (ODF) of the primary axis of the FEP crystals. From the 2D WAXD patterns of either FMWNT/FEP or FEP fibers (Figure 8), the degree of crystal orientation was seen to qualitatively increase with strain during stretching. In this study, the strong (100) crystal diffraction peak on the equator was used to calculate the Hermans' orientation parameter $\bar{P}_2$. The determination of meridional alignment from equatorial measurement was accomplished as follows. Because FEP crystal has a *c*-axis orientation in fiber, the Hermans' orientation parameters $\bar{P}_2$ for the *c*-axis (along the chain axis, $\bar{P}_{2,c}$) could be calculated by the $\bar{P}_2$ value for the *a*-axis ($\bar{P}_{2,a}$) multiplied by a factor of (−2).[23] Results of the Hermans' orientation parameter $\bar{P}_2$ (i.e., $\bar{P}_{2,c}$ in FEP fiber) at different strains are illustrated in Figure 10. Since FEP and FEP/FMWNT nanocomposite fibers were prepared by melt spinning (at a rate of about 5 mpm and with a spin-draw ratio of about 1.0), both polymer chains and FMWNT in the as-spun fibers exhibited a small degree of orientation with a finite value for the Herman's orientation parameter (Figure 10). This was also seen in the corresponding SAXS pattern of the pure FEP fiber, which will be discussed later. It was seen that the $\bar{P}_2$ value increased rapidly at strains below 125%, above which the increase slowed down until the sample was broken. The $\bar{P}_2$ value for the 0.5 wt % FMWNT nanocomposite fiber was slightly lower than that for the pure FEP fiber at strains less than 250%, above which the $\bar{P}_2$ values for both samples were similar, indicating that the small amount of FMWNT (0.5 wt %) only decreased the crystal orientation at lower strains (<250%). On the other hand, the orientation parameter for the 5 wt % FMWNT nanocomposite fiber was much lower than those for FEP and 0.5 wt % FMWNT/FEP fibers. This is because a higher amount of stress can be transferred to the FMWNT phase in the 5 wt % FMWNT fiber than the other two fibers. As the polymer chains experience a reduced level of stress during stretching, the corresponding degree of crystal orientation becomes lower and the corresponding Hermans' orientation parameter becomes smaller. In other words, the higher content of FMWNT in the FEP matrix can bear a larger stress load, but they also impose more physical constraints (since they behave as a rigid nanofibrous network) and lower the mobility of the surrounding chains during stretching.

Orientation of FMWNT. The Hermans' orientation parameter calculated from the (002) reflection in FMWNT was used to follow the orientation of FMWNT in nanocomposite fibers during stretching. In Figure 10, it was seen that the degree of FMWNT orientation in the 5 wt % FMWNT nanocomposite fiber increased with increasing deformation strain. However, the increase of the FMWNT orientation was significantly lower than the increase of the FEP crystal orientation. This can be explained as follows. In 5 wt % of FMWNT nanocomposite fiber, the FMWNT particles were not well dispersed and some even formed clusters (Figure 5). However, the interactions

among the FMWNT particles effectively produced a relatively rigid network (especially with the rigid clusters of FMWNT), which had a much lower compliance (or higher modulus) than that of the semicrystalline FEP matrix. As a result, during deformation, the increase of the FEP crystal orientation is more significant than that of FMWNT orientation.

In-Situ Small-Angle X-ray Scattering Study during Deformation. Selected 2D SAXS patterns of pure FEP fibers at different strains are shown in Figure 11A. The pattern at 0% strain (i.e., the as-spun FEP fiber) exhibited a distinct two-arc pattern with the scattering maxima positioned on the meridian. This scattering feature indicated a partially oriented semicrystalline lamellar structure with the majority of the lamellae arranged perpendicular to the fiber axis, which was consistent with the WAXD results discussed earlier. Upon stretching, some lamellar stacks became tilted (as they were sheared) due to the applied stress, resulting in a four-point pattern in SAXS. The four-point scattering feature was observed at strains below 250%, above which the pattern exhibited an equatorial streak, indicating the formation of a highly oriented fibril-like structure. The evolution of structural change as shown in these SAXS patterns (from two-point to four-point to equatorial streak) is quite common in semicrystalline polymers, such as 6,10 nylon, polyethylene (e.g., UHMWPE), and poly(ethylene terephthalate) (PET).[23,43−45] However, a close comparison of the four-point scattering patterns in FEP during stretching indicated that they were quite different from those in the other polymers, such as UHMWPE[23] and PET.[45] We were somewhat surprised that the data analysis for the four-point patterns of pure FEP was not available in the literature. The lamellar structural evolution of the melt-spun FEP fiber studied by 2D SAXS analysis will thus be discussed first as follows.

Lamellar Structural Evolution of FEP during Stretching by in-Situ SAXS Analysis. A proper analysis of the SAXS four-point patterns should reveal estimates for the long period, the tilt angle of the lamella normals, and possibly other parameters related to size and shape of the lamellar stack as a whole. Currently, there are two popular approaches for the analysis of anisotropic SAXS patterns from oriented semicrystalline polymers: one involves the use of 1D projection along the meridional axis and the subsequent calculation of the correlation function from projected intensity as demonstrated by Strobl et al.,[46] and the other involves the 2D fitting of the entire pattern using elliptical coordinates as demonstrated by Murthy et al.[47] Both approaches have their shortcomings. For instance, the first approach clearly discards some relevant information, such as the tilt of lamella normals and orientation of lamellar stack. In the second approach, the problem is that the description of an anisotropic system in elliptical coordinates is only appropriate if the anisotropy is the result of the affine deformation to an isotropic system. However, the case of the affine deformation may not hold true in typical semicrystalline polymers as shearing effects can cause the orientation of the lamella normals and the shape of the whole lamellar stack to deviate from the ideal situation (as experimentally observed in this study). The goal of the following analysis is thus to take both lamella normal orientation and total stack orientation (and shape) independently into account.

For sufficiently well-defined and narrow four-point patterns, approximations for these parameters could, in principle, be obtained from the positions of the four-peak maxima (and stack size information from their widths). However, for broader scattering maxima this approach will be problematic, especially when the individual distributions of the four-point pattern

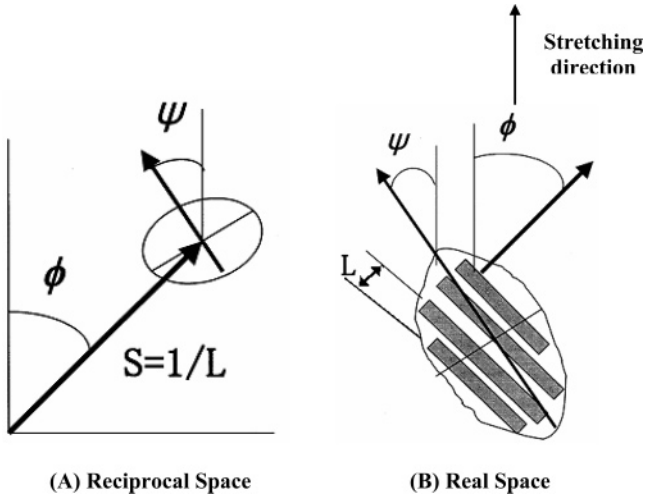

Figure 12. Relationship of the lamellar stack in real space and the scattering intensity distribution in reciprocal space.

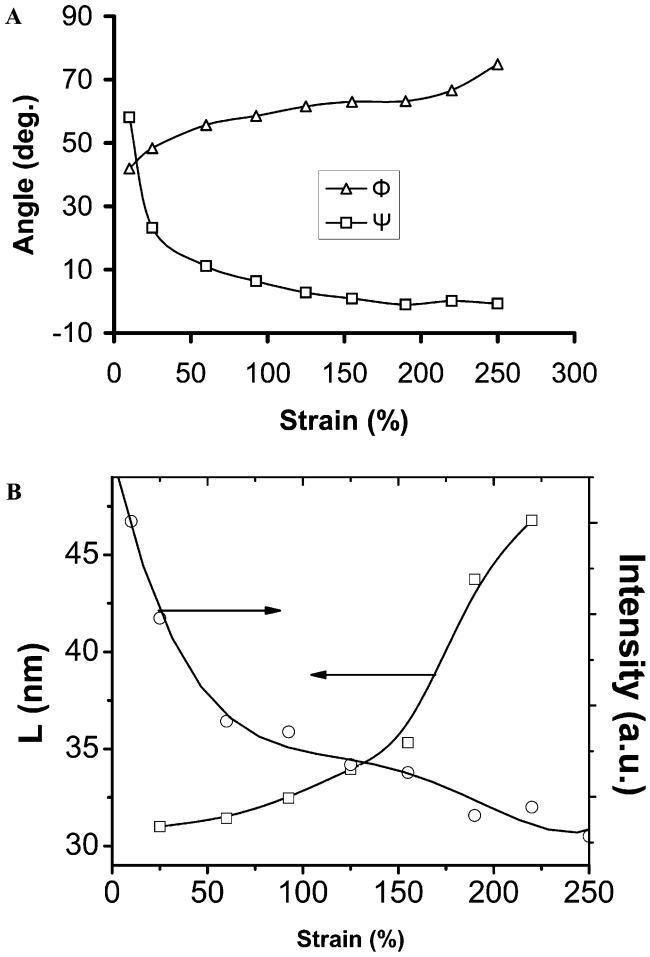

Figure 13. Changes of (A) the angle between the lamellae and lamellar stacks and (B) the long period and the peak intensity in the SAXS pattern at varying strains during stretching of pure FEP fiber at room temperature.

overlap. Under these circumstances, a rigorous treatment of the orientation effects would be costly (in the sense of requiring a lot of numerical integrations). Therefore, we employ a pragmatic approximation outlined in the Appendix, which extracts the parameters of interest, including additional information about the stack size and shape from the 2D fit of the whole four-point pattern. Even though the model is only an approximation, the determination of peak centers and widths from a fit takes

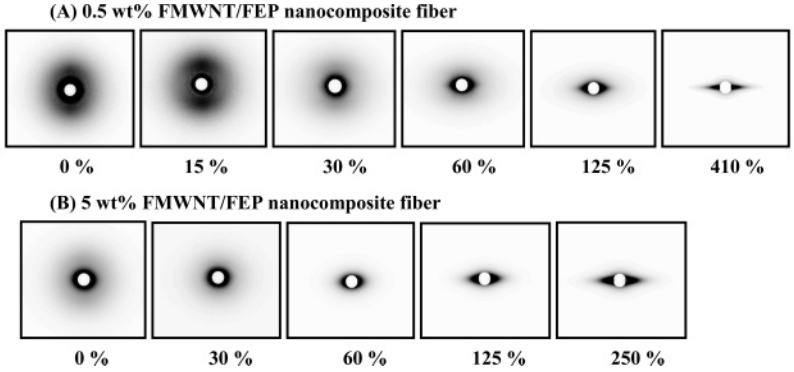

Figure 14. Selected SAXS patterns of the FMWNT/FEP nanocomposite (with 0.5 and 5 wt % FMWNT) fibers at varying strains during stretching at room temperature.

the overlap effects into account, is immune against apparent shifts of the peak maxima, and should lead to reliable parameters and confidence estimates. Below, we demonstrate that results from the SAXS analysis can provide quantitative information on the structural evolution, particularly, the orientation of the lamellae as well as the tilting/shearing of lamella stacks during stretching. This information has offered clues for poor mechanical properties of FEP and enabled us to understand how the presence of FMWNT can possibly affect the lamellar structural change of FEP.

Figure 11B shows the calculated 2D SAXS patterns (at strains from 30% to 250%) using the parameters obtained from the 2D fitting of the experimental data. The goodness of the fit is shown in Figure 11C, where the calculated 3D profile agrees very well with the experimental 3D profile. Several characteristic parameters of the lamellae structure were obtained from the fitting procedure, and they are described as follows.

Figure 12 illustrates the relationship between the scattering profile in reciprocal space and the lamellar structure in real space, where the orientation of the lamellar stack may be different from the orientation of the lamellae within the stack. In this figure, ϕ represents the angle between the lamella normal and the stretching direction, which also corresponds to the angle of the peak shown in reciprocal space; ψ is the angle between the lamellar stack and the stretching direction; L is the long period of the lamellar stack. Figure 13A shows the changes of ϕ and ψ at varying strains during stretching of the FEP fiber at room temperature. It was seen that ϕ increased continuously but rather slowly during stretching, indicating that the lamellae were gradually aligned along the stretching direction (the value of ϕ reached about 70° at a strain of 250%). On the other hand, it was interesting to note that ψ decreased very quickly at strains below 50%, above which the decrease slowed down and ψ reached a value close to 0° at strains above 150%. From the above analysis, two unexpected observations were made: (1) a sudden decrease in the orientation of lamellar stacks at low strains and (2) a nearly perfect alignment of lamellar stacks along the fiber axis at strains above 150%. This behavior is quite different from that observed in UHMWPE[23] or PET[39] during stretching. For example, during the stretching of UHMWPE film at 118 °C, the 2D SAXS patterns exhibited a four-point feature at strains below 600% (i.e., the break point), where the ψ value was found to be almost constant. Clearly the lamellar stacks in highly entangled UHMWPE polymer[23] are very stiff, and they do not tilt or shear during stretching. In contrast, for PET fiber stretching at 90 °C, the ψ value was found to slowly increase instead of decrease in the 100−600% strain range.[45]

The changes of long period and scattered intensity for the FEP fiber during stretching are shown in Figure 13B. The initial long period value (at 0% strain) between the crystal lamellae within the lamellar stack was around 30 nm, which generally agrees with the value reported for the ethylene−propylene (EP) copolymer having the similar morphology.[48] The long period was found to increase in two stages during stretching: a gradual increase at strains below 150% and a rapid increase at strains above 150% (at 250% the long period reached a value of 50 nm). The corresponding scattered intensity from the four-point pattern, which is proportional to the volume fraction of tilted lamellar stacks, was found to rapidly decrease at strains below 50%. The decrease of the scattered intensity slowed down upon further stretching. At 250% strain, the scattered intensity became almost zero, corresponding to the disappearance of the four-point SAXS pattern (Figure 11A). These results are also consistent with the (100) intensity change in WAXD as shown in Figure 9A.

Effect of FMWNT on FEP Lamellar Structural Change. The SAXS patterns obtained during stretching of FMWNT/FEP nanocomposite fibers (Figure 14) were noticeably different from those of the pure FEP fiber (Figure 11A). For 0.5 wt % FMWNT/FEP nanocomposite fiber, the initial SAXS pattern (at 0% strain) exhibited very weak meridional maxima, which became more intense at the initial stage of stretching (e.g., at 15% strain) but completely disappeared at 30% strain, above which only equatorial streaks were observed in the subsequent patterns. The meridional maximum was not at all detected in 2D SXAS patterns of the 5 wt % FMWNT/FEP nanocomposite fiber; the equatorial streak evolved immediately upon stretching and became sharper with increasing strain. The SAXS patterns of the FMWNT/FEP nanocomposite fibers clearly showed that FMWNT greatly affected the FEP morphology. To be specific, FMWNT retarded the tilting of lamellar stacks and the amount of lamellar stacks decreased with the increasing FMWNT content (at 5 wt % FMWNT loading, the lamellar stack morphology was totally absent). Similar results were also observed in several other polymers in the presence of different nanofillers, such as carbon nanofiber, SWNT, and clay.[23,49,50] It is conceivable that at sufficiently high filler concentrations the interactions of nanosized additives would generate a rigid network structure (a scaffold), which not only can carry a significant fraction of stress but also would disrupt the morphology of the matrix. In the system of FMWNT/FEP nanocomposites, even though the total crystallinity of the FEP matrix appeared to be unchanged in the presence of FMWNT (Figure 9), the resulting FEP crystal morphology was more defective, not in a regular stacking mode as evidenced by SAXS. A possible mechanism to explain the effect of FMWNT on the FEP lamellar structural change and the corresponding mechanical behavior is presented as follows.

Both forces of chain−chain interactions as well as segmental friction coefficient are low in FEP (probably similar to polyethylene) due to the nonpolar nature of the molecules. Generally speaking, a much higher molecular weight ($>10^6$ g/mol) is required for fluoropolymers to achieve high mechanical properties through sufficient chain entanglements. This is because the chain length of FEP is significantly shorter than the EP counterpart of the same molecular weight, as the unit molecular mass of FEP is much larger than that of EP. It is logical to assume that the lack of restraints by chain entanglement and the low segmental friction coefficient between the FEP chains allows the slippage and tilting (or shearing) of lamellar stacks even under very low elongation. In a way, the pure FEP behaves as the EP copolymer of a relatively modest chain length.

When FMWNT was added into the FEP matrix, the first effect on the morphology was that very few oriented lamellar stacks formed under the same fiber spinning condition, evident from the SAXS pattern at 0% strain in Figure 14. In fact, at the 5 wt % FMWNT loading, the meridional maxima were not at all detected in the SAXS pattern, indicating that the oriented lamellar stacks almost completely disappeared. As mentioned earlier, because of the good compatibility of the FMWNT surface layer and the FEP matrix, the applied stress would be shared by both FMWNT network and FEP crystal morphology, depending on the FMWNT loading. At low FMWNT content, the crystal morphology of FEP was the dominant component determining the mechanical properties; at high FMWNT content (e.g., 5 wt %), the fibrous network of FMWNT began to bear more mechanical stress. The aggregation of FMWNT would decrease the load transfer of the network to the matrix and increase the rigidity of the filler scaffold. In addition to the FMWNT component, the physical contact between the FEP crystals and FMWNT can also lead to efficient load transfer by simple movement of the FEP crystals and FMWNT, a process that would also absorb the applied load. This was apparent from the observed decrease in the degree of orientation of the FEP crystals in the nanocomposites compared to that in pure FEP.

Conclusions

Oxidized MWNT was modified by reacting 3-perfluorooctylpropylamine with carboxylic acid groups on the tube surface and generating a dense layer of alkane fluoride chains. The modification was confirmed by TGA, TEM, and solubility tests in a perfluorodecalin solvent. The attached fluoride chains greatly improve the compatibility of FMWNT with FEP, whereby good dispersibility of FMWNT in the matrix can be achieved by simple melt-blending. The yield strength and modulus of the nanocomposite fibers all increase with the FMWNT content, but the elongation-to-break ratio decreases. The evolution of the FMWNT orientation and FEP crystal structure and morphology during stretching was studied by in-situ SAXS and WAXD techniques. In FEP fiber, the partially oriented lamellar stacks (with their normals parallel to the fiber axis) can be easily tilted (or sheared) by stretching at low strains. At strains below 250%, the crystallinity decreases with strain due to the chain-pulling mechanism, whereas at strains above 250%, a small degree of strain-induced crystallization takes place. The relatively weak mechanical properties of the melt-spun FEP fiber can be attributed to the low effective chain length or low degree of chain entanglement. The lamellar stack morphology was not observed in the FMWNT/FEP nanocomposite fibers at high FMWNT contents. The mechanical properties of the high loading FMWNT nanocomposite are primarily dictated by the low compliance of the network structure formed by FMWNT, where the filler aggregation would increase the rigidity of the network and decrease the elongation-to-break ratio.

Acknowledgment. The financial support of this work was provided by the Department of Energy (DEFG0286ER45237.023 and DEFG0299ER45760), the Office of Naval Research (N000140310932), and the National Science Foundation (DMR0454887, DMR9984102, and DMR0098104). Acknowledgment is also made to the American Chemical Society, Petroleum Research Fund (38948-AC7), for partial support of this research.

Appendix. 2D SAXS Analysis Schemes

A simple and pragmatic approach was used to analyze the four-point SAXS pattern from FEP. In this approach, a 2D peak profile, $h_0(x,y)$, aligned and centered at the origin, can be factorized into two 1D peak distributions h_x and h_y.

$$h_0(x,y) = h_x(x)\, h_y(y) \tag{1}$$

Each distribution is assumed to be normalized (i.e., $\int_{-\infty}^{\infty} h_j(x)\, dx = 1$, $j = x, y$), so that h_0 is normalized as well ($\int_{-\infty}^{\infty}\int_{-\infty}^{\infty} h_0(x,y)\, dx\, dy = 1$). Typical choices for the 1D distributions h_j are either Gaussian or Lorentzian functions. When they are normalized to unity integral width ($\int h_j(x)\, dx / h_j(0) = 1$), these distributions can be expressed as

$$h_G = \exp(-\pi x^2) \tag{2}$$

$$h_L = (1 + \pi^2 x^2)^{-1} \tag{3}$$

The distributions with adjustable integral width w_j can be expressed as

$$h_j(x) = w_j^{-1} h_J(x/w_j), \quad j = x, y;\ J = G \text{ or } L \tag{4}$$

with h_j as well as h_0 being normalized. The 2D peak profile h_0 can be tilted in place by an angle ϕ through the operation of a rotation tensor

$$\mathbf{T}_\psi = \begin{pmatrix} \cos\psi & -\sin\psi \\ \sin\psi & \cos\psi \end{pmatrix} \tag{5}$$

resulting in a tilted 2D peak profile h_ψ, still centered at the origin.

$$h_\psi(x,y) = h_0\left[\mathbf{T}_\psi \begin{pmatrix} x \\ y \end{pmatrix}\right] \tag{6}$$

To generate a four-point pattern, the distribution h_ψ is replicated four times at positions $(\pm x_0, \pm y_0)$ (or using a polar representation based on $r = \sqrt{{x_0}^2 + {y_0}^2}$ and $\phi = a\tan(x_0/y_0)$), taking the centrosymmetry of the pattern into account, leading to

$$h(x,y) = h_\psi(x - x_0, y - y_0) + h_{-\psi}(x + x_0, y - y_0) + h_{-\psi}(x - x_0, y + y_0) + h_\psi(x + x_0, y + y_0) \tag{7}$$

For a four-point pattern generated by the tilted or sheared lamellar stacks, where the lamellae can have a certain degree of orientation with respect to the fiber axis, the peak position parameters in their polar representation r and ϕ are directly related to the reciprocal long period and to the tilt of lamella normal, respectively, while the peak width and tilt parameters

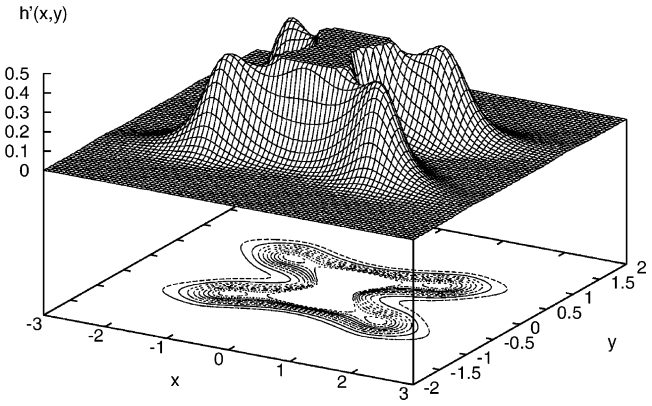

Figure 15. Simulation of the four-point SAXS 2D pattern (bottom) and 3D profiles (top) using eqs 7 and 8.

w_x, w_y, and ψ are related to the size and shape of the lamellar stack. For a more realistic behavior, especially when using a slowly decaying Lorentz distribution h_L, it can be helpful to apply a quadratically decreasing factor

$$h'(x,y) = h(x,y)/(x^2 + y^2) \tag{8}$$

A typical calculation of the 2D four-point pattern (bottom) and 3D intensity profiles (top) using the above approach with a certain choice of parameters is shown in Figure 15.

It should be noted that the usually present fiber symmetry breaks the normalization property of the factorized 2D peaks, so that when normalization is important, the distribution needs to be renormalized for the cylindrical case. Nevertheless, the 1D integral widths w_j still appear to be reasonable measures of the peak properties and, accordingly, reasonable estimates for reciprocal crystallite/stack dimensions and tilted angles.

References and Notes

(1) Hone, J.; Batlogg, B.; Benes, Z.; Johnson, A. T.; Fischer, J. E. *Science* **2000**, *289*, 1730.
(2) Yu, M.; Lourie, O.; Dyer, M. J.; Moloni, K.; Kelly, T. F.; Ruoff, R. S. *Science* **2000**, *287*, 637.
(3) Wang, X.; Chen, X.; Yoon, K.; Fang, D.; Hsiao, B. S.; Chu, B. *Environ. Sci. Technol.* **2005**, *39*, 7684.
(4) Tervoort, T.; Visjager, J.; Graf, B.; Smith, P. *Macromolecules* **2000**, *33*, 6460.
(5) Tervoort, T. A.; Visjager, J. F.; Smith, P. *J. Fluorine Chem.* **2002**, *114*, 133.
(6) Gangal, S. V. Tetrafluoroethylene Polymers. In *Encyclopedia of Polymer Science and Engineering*, 2nd ed.; Mark, H. F., Bikales, N. M., Overberger, G. G., Menges, G., Eds.; Wiley: New York, 1989; Vol. 16, p 577.
(7) Banks, R. E.; Willoughby, B. G. Fluoropolymers. In *The Encyclopedia of Advanced Materials*; Bloor, D., Brook, R. J., Fleming, M. C., Mahajan, S., Eds.; Pergamon Press: Oxford, 1994; Vol. 2, p 862.
(8) Brandrup, J.; Immergut, E. H.; Grulke, E. A. *Polymer Handbook*, 4th ed.; John Wiley & Sons: New York, 1999; VI, p 524.
(9) Sun, Y.-P.; Fu, K.; Lin, Y.; Huang, W. *Acc. Chem. Res.* **2002**, *35*, 1096.
(10) Geng, H.; Rosen, R.; Zheng, B.; Shimoda, H.; Fleming, L.; Liu, J.; Zhou, O. *Adv. Mater.* **2002**, *14*, 1387.
(11) Qin, Y.; Liu, L.; Shi, J.; Wu, W.; Zhang, J.; Guo, Z.; Li, Y.; Zhu, D. *Chem. Mater.* **2003**, *15*, 3256.
(12) Paiva, M. C.; Zhou, B.; Fernando, K. A. S.; Lin, Y.; Kennedy, J. M.; Sun, Y.-P. *Carbon* **2004**, *42*, 2849.
(13) Nakajima, T.; Kasamatsu, S.; Matsuo, Y. *Eur. J. Solid State Inorg. Chem.* **1996**, *33*, 831.
(14) Hattori, Y.; Watanabe, Y.; Kawasaki, S.; Okino, F.; Pradhan, B. K.; Kyotani, T.; Tomita, A.; Touhara, H. *Carbon* **1999**, *37*, 1033.
(15) Okotrub, A. V.; Yudanov, N. F.; Chuvilin, A. L.; Asanov, I. P.; Shubin, Y. V.; Bulusheva, L. G.; Gusel'nikov, A. V.; Fyodorov, I. S. *Chem. Phys. Lett.* **2000**, *322*, 231.
(16) Yudanov, N. F.; Okotrub, A. V.; Shubin, Y. V.; Yudanova, L. I.; Bulusheva, L. G.; Chuvilin, A. L.; Bonard, J.-M. *Chem. Mater.* **2002**, *14*, 1472.
(17) Mickelson, E. T.; Huffman, C. B.; Rinzler, A. G.; Smalley, R. E.; Hauge, R. H.; Margrave, J. L. *Chem. Phys. Lett.* **1998**, *296*, 188.
(18) Watanabe, N.; Nakajima, T.; Touhara, H. *Graphite Fluorides*; Elsevier: Amsterdam, 1988; p 246.
(19) Mickelson, E. T.; Chiang, I. W.; Zimmerman, J. L.; Boul, P. J.; Lozano, J.; Liu, J.; Smalley, R. E.; Hauge, R. H.; Margrave, J. L. *J. Phys. Chem. B* **1999**, *103*, 4318.
(20) Zhang, L.; Kiny, V. U.; Peng, H.; Zhu, J.; Lobo, R. F. M.; Margrave, J. L.; Khabashesku, V. N. *Chem. Mater.* **2004**, *16*, 2055.
(21) Dunitz, J. D.; Taylor, R. *Eur. J. Chem.* **1997**, *3*, 89.
(22) Howard, J. A. K.; Hoy, V. J.; O'Hagan, D.; Smith, G. T. *Tetrahedron* **1996**, *52*, 12613.
(23) Chen, X.; Yoon, K.; Burger, C.; Sics, I.; Fang, D.; Hsiao, B. S.; Chu, B. *Macromolecules* **2005**, *38*, 3883.
(24) Radler, M. J.; Landes, B. G.; Nolan, D. J.; Broomall, C. F.; Chritz, T. C.; Rudolf, P. R.; Mills, M. E.; Bubeck, R. A. *J. Polym. Sci., Part B: Polym. Phys.* **1994**, *32*, 2567.
(25) Nolan, S. J.; Broomall, C. F.; Bubeck, R. A.; Radler, M. J.; Landes, B. G. *Rev. Sci. Instrum.* **1995**, *66*, 2652.
(26) Ran, S.; Burger, C.; Fang, D.; Zong, X.; Chu, B.; Hsiao, B. S.; Ohta, Y.; Yabuki, K.; Cunniff, P. M. *Macromolecules* **2002**, *35*, 9851.
(27) Chu, B.; Hsiao, B. S. *Chem. Rev.* **2001**, *101*, 1727.
(28) Ran, S.; Wang, Z.; Burger, C.; Chu, B.; Hsiao, B. S. *Macromolecules* **2002**, *35*, 10102.
(29) Hu, H.; Bhowmik, P.; Zhao, B.; Hamon, M. A.; Itkis, M. E.; Haddon, R. C. *Chem. Phys. Lett.* **2001**, *345*, 25−28.
(30) Huang, W.; Fernando, S.; Allard, L. F.; Sun, Y.-P. *Nano Lett.* **2003**, *3*, 565.
(31) Fernando, K. A. S.; Lin, Y.; Sun, Y. P. *Langmuir* **2004**, *20*, 4777.
(32) Starkweather, H. W.; Zoller, P., Jr.; Jones, G. A.; Vega, A. J. *J. Polym. Sci., Polym. Phys. Ed.* **1982**, *20*, 751.
(33) Yamamoto, T.; Hara, T. *Polymer* **1982**, *23*, 521.
(34) Weeks, J. J.; Clark, E. S.; Eby, R. K. *Polymer* **1981**, *22*, 1480.
(35) Okuyama, H.; Kanamoto, T.; Porter, R. S. *J. Mater. Sci.* **1994**, *29*, 6485.
(36) White, M. L.; Waddon, A. J.; Atkins, E. D. T.; Farris, R. J. *J. Polym. Sci., Part B: Polym. Phys.* **1998**, *36*, 2811.
(37) Weeks, J. J.; Sanchez, I. C.; Eby, R. K.; Poser, C. I. *Polymer* **1980**, *21*, 325.
(38) Weeks, J. J.; Eby, R. K.; Clark, E. S. *Polymer* **1981**, *22*, 1496.
(39) Marega, C.; Marigo, A.; Carbuglio, C.; Fichera, A.; Martorana, A.; Zannetti, R. *Makromol. Chem.* **1989**, *190*, 1425.
(40) Villani, V.; Pucciariello, R.; Fusco, R.; Marega, C.; Marigo, A.; Zannetti, R. *Makromol. Chem.* **1990**, *191*, 1143.
(41) Pucciariello, R.; Villani, V.; de Ballesteros, O. R. *Macromolecules* **2001**, *34*, 1764.
(42) Kanamoto, T.; Ohama, T.; Tanaka, K.; Takeda, M.; Porter, R. S. *Polymer* **1987**, *28*, 1517.
(43) Arnett, L. M.; Meibohm, E. P. H.; Smith, A. F. *J. Polym. Sci.* **1950**, *5*, 737.
(44) Meibohm, E. P. H.; Smith, A. F. *J. Polym. Sci.* **1951**, *7*, 449.
(45) Kawakami, D.; Hsiao, B. S.; Ran, S.; Burger, C.; Avila-Orta, C.; Sics, I.; Kikutani, T.; Jacob, K.; Chu, B. *Macromolecules* **2005**, *38*, 91.
(46) Strobl, G. R.; Schneider, M. *J. Polym. Sci., Polym. Phys.* **1980**, *18*, 1343.
(47) Murthy, N. S.; Grubb, D. T.; Zero, K. *Macromolecules* **2000**, *33*, 1012.
(48) Liu, L.; Hsiao, B. S.; Fu, B. X.; Ran, S.; Toki, S.; Chu, B.; Tsou, A. H.; Agarwal, P. K. *Macromolecules* **2003**, *36*, 1920.
(49) Levi, N.; Czerw, R.; Xing, S.; Iyer, P.; Carroll, D. L. *Nano Lett.* **2004**, *4*, 1267.
(50) Nam, P. H.; Maiti, P.; Okamoto, M.; Kotaka, T.; Hasegawa, N.; Usuki, A. *Polymer* **2001**, *42*, 9633.

MA060173U